International Journal of Fatigue 82 (2016) 146–157

Contents lists available at ScienceDirect

International Journal of Fatigue

journal homepage: www.elsevier.com/locate/ijfatigue

Non-proportional hardening models for predicting mean and peak stress evolution in multiaxial fatigue using Tanaka's incremental plasticity concepts

Marco Antonio Meggiolaro [a,*], Hao Wu [b], Jaime Tupiassú Pinho de Castro [a]

[a] Department of Mechanical Engineering, Pontifical Catholic University of Rio de Janeiro, Rua Marquês de São Vicente 225 – Gávea, Rio de Janeiro, RJ 22451-900, Brazil
[b] School of Aerospace Engineering and Applied Mechanics, Tongji University, 1239 Siping Road, Shanghai, PR China

ARTICLE INFO

Article history:
Received 15 November 2014
Received in revised form 22 July 2015
Accepted 27 July 2015
Available online 14 September 2015

Keywords:
Multiaxial fatigue
Non-proportional loadings
Non-proportionality factor
Additional NP hardening

ABSTRACT

Non-proportional (NP) hardening can have a significant effect on multiaxial fatigue lives due to the increase in mean and peak stresses it can cause when compared to proportional loads of similar range. Its effect depends both on the material and on the load history path, quantified respectively by the additional NP hardening coefficient α_{NP} and the NP factor F_{NP}. However, since F_{NP} depends on the load path, it is not easy to evaluate under complex multiaxial loading conditions. So, several estimates for the steady-state value of F_{NP} have been proposed to deal with such cases, based on enclosing ellipses or on integrals calculated along the stress, strain, or plastic strain path. Tanaka's incremental plasticity model, on the other hand, is able to predict the NP hardening evolution as a function of the accumulated plastic strain p along any load history, based on the concept of a polarization tensor $[P_T]$ that can be correlated to an internal dislocation structure. In this work, it is shown that the eigenvectors of $[P_T]$ represent principal directions along which dislocation structures may form, whose intensity is quantified by the respective eigenvalues. Two new integral estimates for the steady-state F_{NP} of periodic load histories are proposed, one that exactly reproduces the incremental plasticity predictions from Tanaka's model, and a simpler version calculated solely as a function of the eigenvalues of $[P_T]$. Both can be readily used in fatigue design to correctly account for the additional mean or peak stress effects induced by NP periodic histories. For general non-periodic multiaxial histories, it is also shown that Tanaka's model can be expressed as an evolution equation for $F_{NP}(p)$. Tension–torsion experiments with 316L steel tubular specimens under especially selected discriminating square NP strain paths are conducted to validate the proposed models.

1. Introduction

Some materials can strain-harden much more than it would be expected from the uniaxial cyclic $\sigma\varepsilon$ curve when subjected non-proportional (NP) multiaxial cyclic loads. This phenomenon, called NP hardening, cross-hardening, or additional (NP) strain hardening, depends on the load history, through the NP factor F_{NP}, where $0 \leqslant F_{NP} \leqslant 1$, and on the material, through the additional hardening coefficient α_{NP} (typically $0 \leqslant \alpha_{NP} \leqslant 1$). NP hardening is usually modeled using the exponent h_c from the uniaxial cyclic Ramberg–Osgood equation, see Fig. 1(left), assuming h_c does not vary while the hardening coefficient is gradually increased from H_c to the NP hardening coefficient under NP multiaxial loads

$$H_{NP} = H_c \cdot (1 + \alpha_{NP} \cdot F_{NP}) \tag{1}$$

Defining S_{YNP} as the stabilized NP yield strength associated with a 0.2% plastic strain amplitude, the same value adopted in the monotonic S_Y and cyclic S_{Yc} yield strength definitions, it follows that

$$S_{YNP} = S_{Yc} \cdot (1 + \alpha_{NP} \cdot F_{NP}) \tag{2}$$

since the cyclic and NP hardening exponents are assumed to be equal.

Note that the NP hardening effect can multiply the uniaxial cyclic coefficient H_c, and therefore the cyclic yield strength S_{Yc}, by a factor as high as $(1 + 1 \cdot 1) = 2$, as shown in Fig. 1(right) for a 304 austenitic stainless steel [1]. This figure compares elastoplastic hysteresis loops produced by a NP out-of-phase tension–torsion history and a proportional history, both induced by the same normal strain amplitude $\Delta\varepsilon/2 \cong 0.4\%$. In other words, in the NP history,

* Corresponding author. Tel.: +55 21 3527 1424; fax: +55 21 3527 1165.
E-mail addresses: meggi@puc-rio.br (M.A. Meggiolaro), wuhao@tongji.edu.cn (H. Wu), jtcastro@puc-rio.br (J.T.P. de Castro).

http://dx.doi.org/10.1016/j.ijfatigue.2015.07.027
0142-1123/

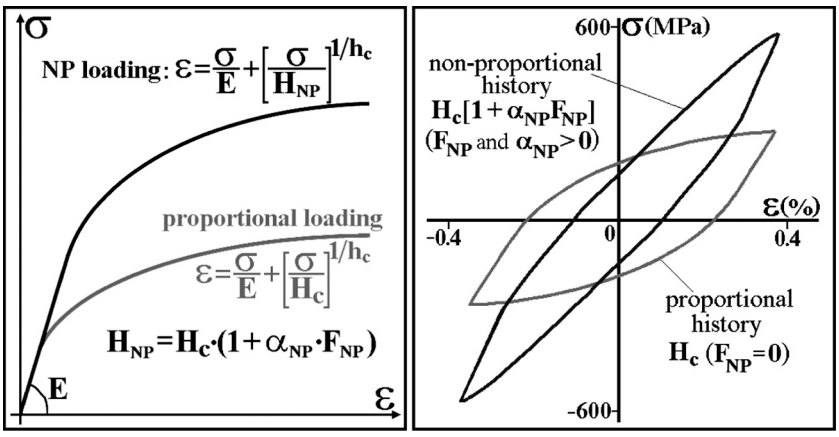

Fig. 1. Effect of cyclic NP loadings on the NP hardening (left) and proportional and NP loops caused by the same range $\Delta\varepsilon$ in AISI 304 steel (right) [1].

the yield surface radius gradually increases from an isotropic hardening value in-between S_Y and S_{Yc} to its NP-hardened yield strength S_{YNP}.

When NP hardening is significant, NP multiaxial load histories can produce fatigue lives that are much shorter than the ones obtained under uniaxial or proportional multiaxial load histories with the same strain range $\Delta\varepsilon$, since NP hardening increases the corresponding $\Delta\sigma$ range. Therefore, calculations based on strain-controlled NP histories, as found in εN specimen tests or around sharp notch tips, must account for NP hardening effects to avoid non-conservative life predictions. Conversely, fatigue lives under stress-controlled histories, as found in SN specimen tests, around mild notch tips or in un-notched components that work under imposed loads, not displacements, can be much higher under NP multiaxial loads than under uniaxial or proportional multiaxial loads with the same range $\Delta\sigma$, due to the lower strain range $\Delta\varepsilon$ necessary to achieve this $\Delta\sigma$ because of the NP hardening effect.

Indeed, the fatigue life associated with the strain-controlled NP loading from Fig. 1(right) can be orders of magnitude shorter than under proportional loading, even though both have the same normal strain amplitude $\Delta\varepsilon/2 \cong 0.4\%$. This large difference is caused by the maximum normal stress in the NP history, which is about twice the value from the proportional history, further opening the initiating microcracks and thus lowering the fatigue crack initiation life.

However, Coffin-Manson's strain-life equation or its Morrow's variations that include mean stresses σ_m would not be able to predict this difference, even if extended from an uniaxial to a multiaxial critical-plane approach formulation, because in both hysteresis loops from Fig. 1(right) the mean stress is null, $\sigma_m = 0$. On the other hand, the multiaxial critical-plane version of Smith–Watson–Topper's (SWT) model, also called SWT-Bannantine [2], would account for this NP hardening effect on the fatigue life, because its damage parameter depends on both $\Delta\varepsilon$ and the maximum σ_{max}, not on σ_m. Therefore, among these three traditional models only SWT would predict, as expected, a shorter fatigue crack initiation life in the presence of higher peak stresses σ_{max} induced by NP hardening. This is not a surprise, since physically speaking σ_{max} is a fatigue driving force whereas σ_m is not. This fact implies that the use of traditional εN equations, which were developed to model uniaxial fatigue problems, can be non-conservative for NP strain-controlled loading histories even when extended to multiaxial conditions. Obviously, such non-conservative errors are inadmissible both for mechanical design and for structural integrity evaluation purposes, meaning that they are simply unacceptable for practical applications, the really important engineering reason for spending time studying such problems.

As mentioned above, NP hardening is not only material-dependent, through α_{NP}, but also load-path dependent, through the NP factor F_{NP}. Uniaxial or proportional multiaxial load histories do not lead to NP hardening, resulting in $F_{NP} = 0$. On the other hand, the largest NP hardening effect occurs when $F_{NP} = 1$, e.g. under a properly scaled 90° out-of-phase tension–torsion loading that generates a circle in the von Mises stress $\sigma \times \tau\sqrt{3}$ or strain $\varepsilon \times \gamma/\sqrt{3}$ diagrams. For a general tension–torsion history, F_{NP} is usually estimated from the aspect ratio of an ellipse that encloses the stress or strain paths in their von Mises diagrams. There are other F_{NP} estimates, e.g. those proposed by Itoh et al. [3] and Bishop [4]. These F_{NP} estimations were compared in [5], where an alternative easier to use yet more powerful F_{NP} estimation model was introduced, based on a simple Moment Of Inertia (MOI) integral equation of the plastic strain path represented in a 5D deviatoric space E_{5p}:

$$\begin{cases} \vec{e}'_{pl} \equiv [\, e_{1pl} \quad e_{2pl} \quad e_{3pl} \quad e_{4pl} \quad e_{5pl} \,]^T, \; e_{1pl} \equiv \varepsilon_{xpl} - (\varepsilon_{ypl} + \varepsilon_{zpl})/2, \\ e_{2pl} \equiv (\varepsilon_{ypl} - \varepsilon_{zpl})\frac{\sqrt{3}}{2}, \; e_{3pl} \equiv \gamma_{xypl}\frac{\sqrt{3}}{2}, \; e_{4pl} \equiv \gamma_{xzpl}\frac{\sqrt{3}}{2}, e_{5pl} \equiv \gamma_{yzpl}\frac{\sqrt{3}}{2} \end{cases} \tag{3}$$

where ε_{xpl}, ε_{ypl}, ε_{zpl}, γ_{xypl}, γ_{xzpl} and γ_{yzpl} are the plastic components of the normal and shear strains.

Note that this 5D deviatoric space is more appropriate to define an integral equation to estimate F_{NP} because, contrary to the stress space used in Bishop's method [4], it is intrinsically independent of the hydrostatic stress component, which does not affect the plastic behavior of most alloys used for structural engineering applications. Moreover, note as well that this $\vec{e}'_{pl}$ vector is equal to the 5D representation of plastic strains proposed by Tanaka [6] multiplied by 3/2:

$$\vec{e}'_{pl} = \frac{3}{2} \cdot \underbrace{\left[e_{x_{pl}} \quad \frac{e_{x_{pl}}+2e_{y_{pl}}}{\sqrt{3}} \quad \frac{\gamma_{xy_{pl}}}{\sqrt{3}} \quad \frac{\gamma_{xz_{pl}}}{\sqrt{3}} \quad \frac{\gamma_{yz_{pl}}}{\sqrt{3}} \right]^T}_{\text{Tanaka's 5D deviatoric space}} \tag{4}$$

since the identity $e_{xpl} + e_{ypl} + e_{zpl} = 0$ implies that $e_{ypl} - e_{zpl} = e_{xpl} + 2e_{ypl}$.

In fact, there are at least six motivations to prefer the 5D projection $\vec{e}'_{pl}$ of the plastic strain space to calculate F_{NP}, instead of a stress space, total strain space, or even the 6D plastic strain space:

(i) this projection is a non-redundant representation of the plastic strains, since the linear dependency $e_{xpl} + e_{ypl} + e_{zpl} = 0$ is automatically removed when projecting the 6D strains onto this 5D deviatoric sub-space E_{5p};
(ii) for either free-surface conditions, un-notched tension–torsion, or uniaxial load histories, respectively 3D, 2D, or 1D sub-spaces of this 5D representation could be used, significantly decreasing its computational cost. Voigt-Mandel's 6D deviatoric representation, on the other hand, would need to use a 3D formulation even under uniaxial conditions in x, since the non-zero ε_{ypl} and ε_{zpl} (due to plastic Poisson effects) and ε_{xpl} would be present in all three normal deviatoric components. On the other hand, a 1D representation from $e_{1pl} \equiv \varepsilon_{xpl} - (\varepsilon_{ypl} + \varepsilon_{zpl})/2$ would be enough in the uniaxial case, because $e_{2pl} \equiv (\varepsilon_{ypl} - \varepsilon_{zpl})\sqrt{3}/2 = 0$ (since $\varepsilon_{ypl} = \varepsilon_{zpl} = -\bar{\nu} \cdot \varepsilon_{ypl}$, where $\bar{\nu}$ is the effective Poisson ratio, a weighted mean of the elastic ν and plastic 0.5 Poisson ratios) and all shear $e_{3pl} \equiv \gamma_{xypl}\sqrt{3}/2$, $e_{4pl} \equiv \gamma_{xzpl}\sqrt{3}/2$ and $e_{5pl} \equiv \gamma_{yzpl}\sqrt{3}/2$ would be zero as well;
(iii) similarly to the $\vec{e}'$ projection, $\vec{e}'_{pl}$ is also independent of the hydrostatic strain ε_h, since it is a 5D projection of a deviatoric space as well, compatible with the expected independence between F_{NP} and ε_h (since F_{NP} depends only on plastic strains);
(iv) the scaled down version $(2/3) \cdot \vec{e}'_{pl}$ of this projection is identical to Tanaka's 5D plastic strain vector defined in [6], which has been shown to be appropriate to evaluate the NP hardening evolution in incremental plasticity calculations;
(v) the Euclidean norm $(2/3) \cdot |\vec{e}'_{pl}|$ is equal to the von Mises plastic equivalent strain, which provides a convenient metric for the deviatoric plastic strain space associated with this representation; and
(vi) the direction of these 5D strain vectors is related with the principal direction of the loading. This last statement can be observed, for instance, in the calculation of the principal direction angle θ_p with respect to the y axis in the y–z plane

$$\tan 2\theta_p = \gamma_{yz}/(\varepsilon_y - \varepsilon_z) = e_5/e_2 \cong e_{5_{pl}}/e_{2_{pl}} \tag{5}$$

where the approximation $e_5/e_2 \cong e_{5pl}/e_{2pl}$ is valid for large plastic strains, resulting in $\vec{e}' \cong \vec{e}'_{pl}$.

Several incremental plasticity equations make use of the Euclidean norm of the increments of the plastic strain vector, which define infinitesimal variations of $\vec{e}'_{pl}$. One way to account for this norm is through the equivalent plastic strain increment dp, a positive scalar quantity that can be defined as an infinitesimal absolute variation of the plastic von Mises strain $\varepsilon_{pl,Mises} = |\vec{e}'_{pl}|/(1 + 0.5)$, assuming as usual that the plastic strains conserve volume, thus that the plastic Poisson ratio is 0.5. The value of dp can be defined in the 5D plastic strain space E_{5p} from

$$\varepsilon_{pl,Mises} = \frac{2}{3} \cdot \left|\vec{e}'_{pl}\right| \Rightarrow dp = \frac{2}{3} \cdot \left|d\vec{e}'_{pl}\right| \tag{6}$$

The integral of these positive infinitesimal increments dp is defined as the *accumulated plastic strain p*, which in integral form is expressed as

$$p = \int dp = \frac{2}{3} \cdot \int \left|d\vec{e}'_{pl}\right| \tag{7}$$

Note that $\varepsilon_{pl,Mises}$ and p are very different concepts even though they are both intrinsically positive quantities, since the von Mises plastic strain $\varepsilon_{pl,Mises}$ can oscillate during a load cycle, while the accumulated plastic strain p increases monotonically in any deformation process.

In the following sections, Tanaka's NP hardening model is applied to the E_{5p} space to predict the transient evolution of NP hardening, which can be very much important for improving the accuracy of practical multiaxial fatigue life calculations, in particular if this transient period is associated with some ratcheting or mean stress relaxation. From Tanaka's model, an evolution equation for F_{NP} is developed, from which new steady-state F_{NP} estimate equations are derived. These estimates are then experimentally verified from tension–torsion experiments in tubular 316L specimens under NP histories describing square paths in a normal-shear stress diagram, which are particularly sensitive to F_{NP} transients.

2. Tanaka's NP hardening model

Estimates for the steady-state value of F_{NP} have been proposed in [3–5,7]. These estimates are especially useful for periodic NP multiaxial load histories that consist of a few cycles per period, where F_{NP} reaches an approximately constant stabilized value. However, general NP multiaxial load histories have a NP factor $F_{NP}(p)$ that depends on the accumulated plastic strain p and on the previous plastic history, which continually evolves and changes the hardening behavior of materials that have an additional hardening coefficient $\alpha_{NP} > 0$.

It is well known that NP hardening has been related to stacking faults, which are local regions of incorrect stacking of crystal planes [1]. Fig. 2 shows stacking fault examples for HCP (Hexagonal Close-Packed) and for FCC (Face Centered Cubic) lattices. HCP lattices superimpose the various atomic planes following a twofold sequence type **ab-ab-ab-ab-ab**. The stacking fault in the HCP lattice from Fig. 2(top) is caused by the plane arranged in the **c** configuration, causing an interruption of the stacking sequence of the crystal structure, which becomes **ab-ab-abc-ab-ab**. FCC lattices, on the other hand, which usually follow a sequence **abc-abc-abc-abc**, may present stacking faults from the local absence of this **c** configuration, as shown in the sequence **abc-abc-ab-abc** in Fig. 2(bottom). These faults cause the HCP lattice to become locally FCC in the **abc** plane sequence, while the FCC lattice locally becomes HCP in the **ab** region. These planar defects cause lattice incompatibilities that prevent or impair dislocations from switching gliding planes. Moreover, each of these crystallization faults requires a Stacking Fault Energy (SFE) to be generated, measured per unit area in J/m^2. Materials with low SFE very easily develop large stacking faults. For instance, the FCC lattice of 316 austenitic stainless steels requires only about 25 mJ per m^2 to generate them. Screw dislocations associated with plastic straining cannot cross-slip across such large stacking faults, even under high stresses, due to lattice incompatibility. So, the slip bands generated by proportional loadings remain planar, limiting the material ductility. However, in the presence of NP loads, the changes in principal direction allow the activation of cross-slip bands in all directions. An increase in the hardening effect with respect to proportional loadings is thus expected, caused by the change in direction of the maximum shear planes, resulting in an additional hardening coefficient $\boldsymbol{\alpha_{NP} \gg 0}$.

On the other hand, stacking faults are rarely seen in materials with high SFE, such as in most aluminum alloys, which typically require more than 200 mJ per m^2 to induce them. Without the obstruction caused by stacking faults, the screw dislocations may cross-slip even under proportional loadings, giving the material an extra ductility since the many slip systems are able to well distribute the deformation in all possible directions in 3D. Slips of dislocations are wavy, changing their glide planes easily, even for uniaxial histories. Hence, since cross-slip bands already happen naturally even under proportional loadings, NP histories do not

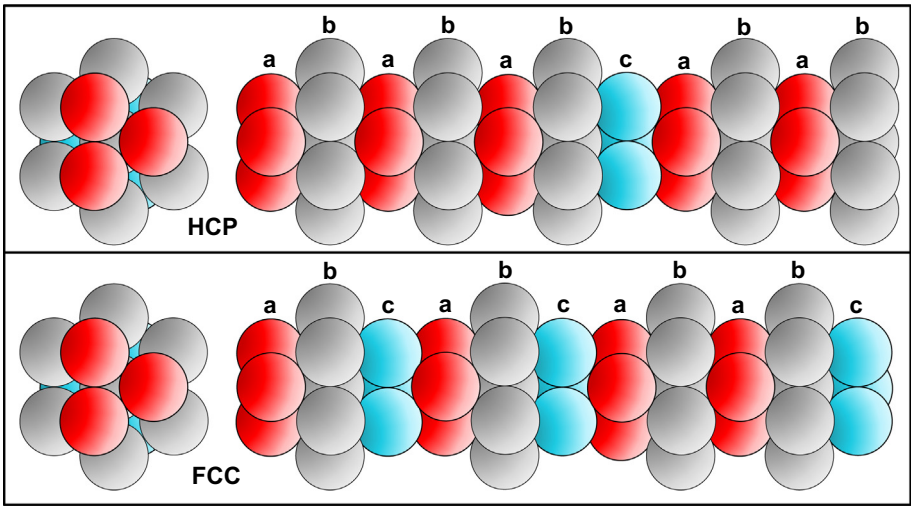

Fig. 2. HCP and FCC lattices with stacking faults.

cause any significant increase in hardening, resulting in $\boldsymbol{\alpha_{NP}} \cong \mathbf{0}$. In summary, the additional hardening coefficient $\boldsymbol{\alpha_{NP}}$ is a parameter that reflects the material sensitivity to the non-proportionality of the loads. Values of α_{NP} are usually high in austenitic stainless steels at room temperature ($\boldsymbol{\alpha_{NP}} \cong \mathbf{1}$ for 316 stainless steel) and very low in aluminum alloys ($\boldsymbol{\alpha_{NP}} \cong \mathbf{0}$ for Al 7075).

In materials with a high α_{NP}, a sequence of NP multiaxial loading cycles causes an additional hardening effect that increases as a function of p and of the non-proportionality of the load, until reaching a steady-state level also known as the target value of $F_{NP}(p)$. Conversely, a long series of proportional loads may cause a "proportional softening" effect that reverts a previous NP hardening process. Incremental plasticity models must account for this transient NP hardening and proportional softening to correctly predict fatigue lives, because these transients can have a significant effect on the resulting strain or stress amplitudes, respectively under stress or strain-controlled conditions in low-cycle fatigue, and a very large effect on ratcheting and on mean stress relaxation problems.

The transient NP hardening model proposed by Tanaka [6] is probably the most widely adopted in modern incremental plasticity calculations. Tanaka defined a polarization tensor $[P_T]$ that can store information on the directionality of the accumulated plastic strains induced by the loading history, which can be proportional or NP. This macroscopic structural tensor is an internal state variable that is able to describe the loading-path-shape dependence of the NP hardening process through the mathematical representation of an internal dislocation structure. The directions stored in this tensor are the ones described by 5D normal unit vectors $\vec{n}'$, which are defined as the direction of the current infinitesimal plastic strain increment $d\vec{e}'_{pl}$ in the 5D E_{5p} plastic strain space. According to the normality rule [8], these unit vectors are perpendicular to the E_{5p} representation of the yield surface during plastic straining.

2.1. Tanaka's polarization tensor

Tanaka's polarization tensor $[P_T]$ in its general case can be represented as a 5×5 matrix. This tensor, which is initially equal to zero, is calculated at each plastic strain increment from the differential equation

$$[dP_T] = (\vec{n}' \cdot \vec{n}'^T - [P_T]) \cdot hr_T \cdot dp \tag{8}$$

where hr_T is a rate that dictates how fast $[P_T]$ evolves as a function of the equivalent plastic strain increment dp. The quantity $\vec{n}' \cdot \vec{n}'^T$ is the *outer product* of $\vec{n}'$, a matrix operator that projects any vector $\vec{v}$ onto $\vec{n}'$, since $\vec{n}' \cdot (\vec{n}'^T \cdot \vec{v}) = (\vec{n}' \cdot \vec{n}'^T) \cdot \vec{v}$. The outer product always results in a singular symmetrical 5×5 matrix with five mutually perpendicular eigenvectors, one of them equal to $\vec{n}'$ and associated with a unit eigenvalue $\lambda_1 = 1$, and all other four associated with null eigenvalues $\lambda_2 = \lambda_3 = \lambda_4 = \lambda_5 = 0$. This matrix is also referred to as the *tensor product* $\vec{n}' \otimes \vec{n}'$. Since the evolution equation of $[P_T]$ only involves symmetrical matrices, it follows that $[P_T]$ itself is symmetric.

The 5×5 version of the polarization tensor $[P_T] = [P_{Tij}]$ $(i, j = 1, \ldots, 5)$ is needed in load histories involving all six plastic strain components. In load histories under free-surface conditions, the normal vector $\vec{n}'$ can be represented in the 3D diagram $e_{1pl} \times e_{2pl} \times e_{3pl}$ from a sub-space $\vec{e}_{3D_{pl}}$, reducing $[P_T]$ to the 3×3 representation

$$[P_T] = \begin{bmatrix} P_{T11} & P_{T12} & P_{T13} \\ P_{T21} & P_{T22} & P_{T23} \\ P_{T31} & P_{T32} & P_{T33} \end{bmatrix}, \text{ with } \vec{e}_{3D_{pl}} \equiv \frac{3}{2} \cdot \left[\varepsilon_{x_{pl}} \quad \frac{\varepsilon_{y_{pl}} - \varepsilon_{z_{pl}}}{\sqrt{3}} \quad \frac{\gamma_{xy_{pl}}}{\sqrt{3}} \right]^T \tag{9}$$

Moreover, $[P_T]$ can be further simplified to a 2×2 representation for tension–torsion histories, where $\vec{n}'$ is represented in the 2D diagram $e_{1pl} \times e_{3pl}$ from the sub-space $\vec{e}_{2D_{pl}}$, resulting in

$$[P_T] = \begin{bmatrix} P_{T11} & P_{T13} \\ P_{T31} & P_{T33} \end{bmatrix}, \text{ and } \vec{e}_{2D_{pl}} \equiv \begin{bmatrix} e_{1_{pl}} & e_{3_{pl}} \end{bmatrix}^T = \frac{3}{2} \cdot \left[\varepsilon_{x_{pl}} \quad \frac{\gamma_{xy_{pl}}}{\sqrt{3}} \right]^T \tag{10}$$

This dimensional reduction down to 2×2 is only possible because of the properties of the adopted 5D plastic strain space E_{5p}, which was one of the six motivations listed in the last section to adopt it.

The polarization tensor can be used to model the cross-hardening effect, see Fig. 3, which shows the transient behavior $H(p)/H_c$ of the Ramberg–Osgood hardening coefficient $H(p)$ for materials with $\alpha_{NP} > 0$, where H_c is the cyclically-stabilized uniaxial hardening coefficient. In this example, a virgin specimen is initially cycled in tension–compression, until the accumulated plastic strain reaches some value $p = p_a$. During this process, isotropic hardening causes the hardening

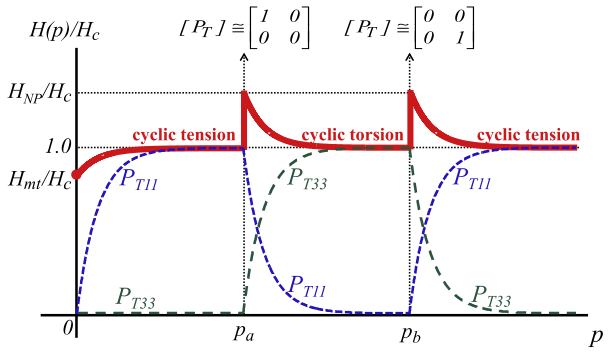

Fig. 3. Variation of the hardening coefficient $H(p)$ due to cross-hardening effects in materials with additional hardening coefficient $\alpha_{NP} > 0$, adapted from [6].

coefficient to gradually change from its monotonic value H_{mt} to the cyclically-stabilized one H_c. For simplicity, in this initial example it is assumed that both monotonic and cyclic exponents are not too different, represented by the cyclic value h_c. A uniaxial dislocation structure is then gradually generated in the direction of these tension–compression cycles, represented in $[P_T]$ by

$$[P_T] = \begin{bmatrix} P_{T11} & P_{T13} \\ P_{T31} & P_{T33} \end{bmatrix} = \begin{bmatrix} 1-\exp(-hr_T \cdot p) & 0 \\ 0 & 0 \end{bmatrix}, \text{ for } 0 \leqslant p \leqslant p_a \tag{11}$$

where $exp(x)$ is the exponential function e^x, with $e \cong 2.71828$. This uniaxial dislocation structure is fully formed when the first element of $[P_T]$ converges to its target value $P_{T11} = 1$, see Fig. 3, resulting in a unit eigenvalue associated with an eigenvector in the normal direction e_{1pl}.

Then, if the tension–compression cycles are replaced by cyclic torsion, this change causes a sudden increase in the transient hardening coefficient from the uniaxial H_c to the NP value H_{NP} (if the material has $\alpha_{NP} > 0$). This sudden strain-hardening is explained by the cross-hardening effect caused by the uniaxial dislocation structure formed in the preceding tension–compression cycles, represented by $P_{T11} = 1$, which resists much more to the mismatched torsional loads than to previous tensile loads. But the torsional cycles gradually destroy this uniaxial tension–compression dislocation structure, making P_{T11} tend toward zero, as seen in Fig. 3 for the interval $p_a \leqslant p \leqslant p_b$, which allows the material to soften again from H_{NP} to H_c. Meanwhile, a new dislocation structure is gradually generated in the torsional direction through P_{T33}, leading to the $[P_T]$ solution

$$[P_T] \cong \begin{bmatrix} \exp[-hr_T \cdot (p-p_a)] & 0 \\ 0 & 1-\exp[-hr_T \cdot (p-p_a)] \end{bmatrix}, \quad \text{for } p_a \leqslant p \leqslant p_b \tag{12}$$

The torsional dislocation structure is fully formed when P_{T33} converges to its target value $P_{T33} = 1$ near $p = p_b$, see Fig. 3, resulting in a unit eigenvalue for $[P_T]$ associated with an eigenvector in the torsional direction e_{3pl}.

If the torsional cycles are then replaced again with cyclic tension–compression for $p \geqslant p_b$, another sudden increase in the hardening coefficient from H_c to H_{NP} is observed, as also seen in Fig. 3. Now, the tension–compression cycles are resisted by the mismatched torsional dislocation structure formed in the preceding torsional cycles, represented by $P_{T33} = 1$, causing a sudden strain-hardening effect. But this torsional dislocation structure is gradually destroyed as P_{T33} tends toward zero, allowing the material to soften again from H_{NP} to H_c. Meanwhile, P_{T11} starts increasing again toward $P_{T11} = 1$, while the unit eigenvalue of $[P_T]$ becomes associated with the tensile direction e_{1pl}, and the process continues. It can be concluded from this simple example that the eigenvectors of $[P_T]$ represent principal directions along which dislocation structures may form, whose intensity is quantified by the respective eigenvalues, ranging from 0 (no dislocation structures in the considered direction) to 1 (all dislocation structures in this direction).

For general NP multiaxial histories, after several plastic strain increments, Tanaka's polarization tensor $[P_T]$ results in a 5×5 matrix whose eigenvalues $\lambda_{T1} \geqslant \lambda_{T2} \geqslant \cdots \geqslant \lambda_{T5} > 0$ are proportional to the accumulated plastic strains in the direction of each unit eigenvector $\vec{v}_{T1}, \vec{v}_{T2}, \ldots, \vec{v}_{T5}$. So, proportional load histories always result in a polarization tensor $[P_T]$ with only one non-zero eigenvalue, corresponding to the eigenvector parallel to the constant plastic straining direction associated with proportional loading conditions. The other four eigenvalues would either be equal to zero or very close to zero for quasi-proportional histories.

On the other hand, highly NP load histories have at least two dominant (high) eigenvalues λ_{T1} and λ_{T2}. These eigenvalues should be equal ($\lambda_{T1} = \lambda_{T2}$) in the 90° out-of-phase tension–torsion case with equal normal and effective shear amplitudes, i.e. $\Delta\sigma_x/2 = (\Delta\tau_{xy}/2)\cdot\sqrt{3}$. In this case, the plastic straining direction is constantly changed as the load path describes a circle in the $e_{1pl} \times e_{3pl}$ diagram, keeping the cross-hardening effect alive while the transient Ramberg–Osgood coefficient is evolving to reach a target NP value H_{NP} without posterior hardening or softening.

In summary, the eigenvectors and eigenvalues of the target values of the evolution of $[P_T]$ mathematically represent the stabilized internal dislocation structure formed by the loading process. These eigenvalues are also useful to detect reduced dimensionality of such structures, ranging from 1D for proportional histories (with only one non-zero eigenvalue) to 5D if all eigenvalues are significantly higher than zero.

2.2. Non-proportionality parameter

Tanaka's original model [6] indirectly made use of the eigenvalues of $[P_T]$ to estimate F_{NP}, through a non-proportionality parameter A_T given by

$$A_T = \sqrt{1 - \frac{|[P_T]\cdot\vec{n}'|^2}{tr([P_T]^T \cdot [P_T])}} \tag{13}$$

where $tr(X)$ is the trace function that returns the sum of the elements on the main diagonal of a matrix $[X]$. This A_T is in fact a function of the eigenvalues of $[P_T]$, as it will be proven next.

Let's first study the physical meaning of A_T. Since $\lambda_{T1}, \lambda_{T2}, \ldots, \lambda_{T5}$ are the eigenvalues whereas $\vec{v}_{T1}, \vec{v}_{T2}, \ldots, \vec{v}_{T5}$ the unit eigenvectors of $[P_T]$, then $[P_T]\cdot\vec{v}_{Ti} = \lambda_{Ti}\cdot\vec{v}_{Ti}$ with $|\vec{v}_i| = 1$ for all $i = 1, 2, \ldots, 5$. In addition, these unit eigenvectors also constitute an orthonormal system, being mutually perpendicular due to the fact that $[P_T]$ is symmetric. So, these orthonormal eigenvectors form a base in the 5D plastic space E_{5p}, allowing the projection $[P_T]\cdot\vec{n}'$ to be rewritten as

$$\begin{aligned}[P_T]\cdot\vec{n}' &= [P_T]\cdot\sum_{i=1}^{5}(\vec{v}_{Ti}^T\cdot\vec{n}')\cdot\vec{v}_{Ti} = \sum_{i=1}^{5}(\vec{v}_{Ti}^T\cdot\vec{n}')\cdot([P_T]\cdot\vec{v}_{Ti}) \\ &= \sum_{i=1}^{5}(\vec{v}_{Ti}^T\cdot\vec{n}')\cdot\lambda_{Ti}\vec{v}_{Ti}\end{aligned} \tag{14}$$

and thus its squared norm $|[P_T]\cdot\vec{n}'|^2$ becomes

$$\begin{aligned}|[P_T]\cdot\vec{n}'|^2 &= ([P_T]\cdot\vec{n}')^T\cdot([P_T]\cdot\vec{n}') = \sum_{i=1}^{5}\lambda_{Ti}^2(\vec{v}_{Ti}^T\cdot\vec{n}')^2\cdot\underbrace{\vec{v}_{Ti}^T\cdot\vec{v}_{Ti}}_{1} \\ &= \sum_{i=1}^{5}(\lambda_{Ti}\vec{v}_{Ti}^T\cdot\vec{n}')^2\end{aligned} \tag{15}$$

Since the trace of any matrix product $[X]^T[X]$ is always equal to the sum of the squares of the eigenvalues of the original matrix $[X]$, it follows that

$$tr\left([P_T]^T \cdot [P_T]\right) = \lambda_{T1}^2 + \lambda_{T2}^2 + \lambda_{T3}^2 + \lambda_{T4}^2 + \lambda_{T5}^2 \tag{16}$$

Inserting Eqs. (15) and (16) into (13), Tanaka's NP parameter A_T becomes

$$A_T = \sqrt{1 - \frac{\left(\lambda_{T1}\,\vec{v}_{T1}^T\vec{n}'\right)^2 + \left(\lambda_{T2}\,\vec{v}_{T2}^T\vec{n}'\right)^2 + \left(\lambda_{T3}\,\vec{v}_{T3}^T\vec{n}'\right)^2 + \left(\lambda_{T4}\,\vec{v}_{T4}^T\vec{n}'\right)^2 + \left(\lambda_{T5}\,\vec{v}_{T5}^T\vec{n}'\right)^2}{\lambda_{T1}^2 + \lambda_{T2}^2 + \lambda_{T3}^2 + \lambda_{T4}^2 + \lambda_{T5}^2}} \tag{17}$$

So, Tanaka's NP A_T parameter can be interpreted as the root-mean-square (RMS) average of the projections $\vec{v}_{Ti}^T \cdot \vec{n}'$ of the plastic flow direction $\vec{n}'$ onto the eigenvectors $\vec{v}_{Ti}$ of $[P_T]$, weighted by the square of the associated eigenvalues λ_{Ti} ($i = 1, 2, \ldots, 5$). Since these squared unit vector projections $\left(\vec{v}_{Ti}^T \cdot \vec{n}'\right)^2$ are always between 0 and 1, because $\left(\vec{v}_{Ti}^T \cdot \vec{n}'\right)^2 \leqslant |\vec{v}_{Ti}|^2 = 1$, it follows that $0 \leqslant A_T \leqslant 1$.

Consider for instance a proportional load history where λ_{T1} is the only non-zero eigenvalue. So, any plastic flow in the dominant direction $\vec{n}' = \vec{v}_{T1}$ of the proportional load history will result in $A_T = \sqrt{1 - \lambda_{T1}^2/\lambda_{T1}^2} = 0$. On the other hand, a subsequent plastic flow in a direction $\vec{n}'$ perpendicular to this proportional direction (i.e. $\vec{n}' \perp \vec{v}_{T1}$) will instantaneously change the A_T parameter to $A_T = \sqrt{1-0} = 1$. This means that A_T is a varying parameter, usually oscillatory, that measures the *trend* of the plastic flow to induce NP hardening. This sudden increase from $A_T = 0$ to $A_T = 1$ is able to model the sudden cross-hardening effects from the example shown in Fig. 3.

Even though $0 \leqslant A_T \leqslant 1$, the *average* value of this oscillatory A_T along a given periodic loading path always lies between 0 and $1/\sqrt{2}$. The latter extreme value corresponds to a 90° out-of-phase loading, e.g. a tension–torsion circular load history on the $\vec{v}_{T1} \times \vec{v}_{T2}$ plane, which leads to $\lambda_{T1} = \lambda_{T2} \neq 0$ and $\lambda_{T3} = \lambda_{T4} = \lambda_{T5} = 0$, resulting in

$$\begin{aligned} A_T &= \sqrt{1 - \frac{\left(\lambda_{T1}\,\vec{v}_{T1}^T\vec{n}'\right)^2 + \left(\lambda_{T2}\,\vec{v}_{T2}^T\vec{n}'\right)^2}{\lambda_{T1}^2 + \lambda_{T2}^2}} \\ &= \sqrt{1 - \frac{\lambda_{T1}^2}{2\lambda_{T1}^2}\left[\underbrace{\left(\vec{v}_{T1}^T \cdot \vec{n}'\right)^2 + \left(\vec{v}_{T2}^T \cdot \vec{n}'\right)^2}_{1}\right]} = \frac{1}{\sqrt{2}} \end{aligned} \tag{18}$$

because the plastic increment direction $\vec{n}'$ belongs to the $\vec{v}_{T1} \times \vec{v}_{T2}$ plane, which implies that the sum of the squares of its projections $\vec{v}_{T1}^T \cdot \vec{n}'$ and $\vec{v}_{T2}^T \cdot \vec{n}'$ onto the orthonormal directions $\vec{v}_{T1}$ and $\vec{v}_{T2}$ results in $|\vec{n}'|^2$, which is equal to 1 because $\vec{n}'$ is a unit vector.

3. Transient NP hardening

The NP factor F_{NP} is usually adopted to quantify the non-proportionality of periodic multiaxial load histories from its steady-state value, but the transient value $F_{NP}(p)$ of the NP factor must be considered to study its evolution. For a virgin material, it evolves from its initial condition $F_{NP}(0) = 0$, and for periodic histories where each period consists of few cycles, it is expected that $F_{NP}(p)$ converges to the steady-state F_{NP} after a sufficiently large accumulated plastic strain p. Otherwise, for general non-periodic multiaxial histories, $F_{NP}(p)$ might evolve without converging to a specific value.

The NP evolution of $F_{NP}(p)$ can be derived from the evolution of the yield surface radius S (when represented in a 5D deviatoric space based on a von Mises metric, as described in [9,10]) from a cyclically-stabilized yield strength $S = S_{Yc}$ to a target value

$$S = S_{Yt} = S_{Yc} \cdot [1 + \alpha_{NP} \cdot (F_{NPt} + F_{NPmr})] \tag{19}$$

using a transient equation very similar to the one adopted in the Voce rule,

$$dS = (S_{Yt} - S) \cdot hr_{NP} \cdot dp \tag{20}$$

where F_{NPt} is a target value of the NP factor (which can vary at every load cycle, especially for non-periodic histories), F_{NPmr} is a memory factor that stores the permanent NP hardening caused by the previous plastic history, and hr_{NP} is the NP hardening rate which dictates how fast the yield surface radius S changes from its current value to the target S_{Yt}. For simplicity, in this work the memory factor F_{NPmr} is assumed equal to zero, although its value could be calibrated from a 90° out-of-phase tension–torsion loading until stabilization in $F_{NP}(p) = 1$, followed by uniaxial tension–compression cycles that could lower $F_{NP}(p)$ to a non-zero memory factor F_{NPmr}.

Before presenting more detailed equations for describing the target F_{NPt}, let's assume that the solution of the above evolution equation has the form

$$S = S_{Yc} \cdot [1 + \alpha_{NP} \cdot F_{NP}(p)] \tag{21}$$

If Eqs. (19) and (21) are inserted into Eq. (20), then

$$\begin{aligned} dS &= S_{Yc} \cdot \alpha_{NP} \cdot dF_{NP}(p) \\ &= [S_{Yc} \cdot \alpha_{NP}(F_{NPt} + F_{NPmr}) - S_{Yc} \cdot \alpha_{NP} \cdot F_{NP}(p)] \cdot hr_{NP} \cdot dp \end{aligned} \tag{22}$$

which, after canceling out the $S_{Yc} \cdot \alpha_{NP}$ term, results in an evolution equation for the transient NP factor $F_{NP}(p)$, given by $dF_{NP}(p) = [F_{NPt} - F_{NP}(p)] \cdot hr_{NP} \cdot dp$, where $dF_{NP}(p)$ is an infinitesimal variation of $F_{NP}(p)$. This $F_{NP}(p)$ evolution equation is much more convenient than the traditional approach of evolving the radii of the yield surface and all hardening surfaces from a multi-surface or a non-linear kinematic hardening model, which would be more computationally intensive, especially in a global Finite Element formulation. Indeed, in this proposed approach the yield and all hardening surfaces are then automatically expanded (or contracted) from the current $F_{NP}(p)$ value.

The simplest and most commonly adopted version of Tanaka's evolution equation assumes a target value $F_{NPt} = A_T\sqrt{2}$ and a zero memory factor $F_{NPmr} = 0$, from which an $F_{NP}(p)$ evolution equation is derived

$$dF_{NP}(p) = \left[A_T\sqrt{2} - F_{NP}(p)\right] \cdot hr_{NP} \cdot dp \tag{23}$$

Note that, for a constant target F_{NPt}, a constant steady-state value $F_{NP}(p) = F_{NPt} = A_T\sqrt{2}$ is asymptotically reached as the increments $dF_{NP}(p)$ tend toward zero. Fig. 4 shows the evolution

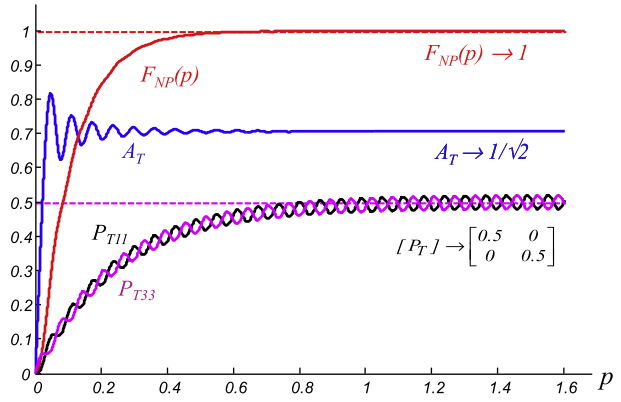

Fig. 4. Evolution of $[P_T]$, A_T and $F_{NP}(p)$ for a 90° out-of-phase tension–torsion loading.

of $F_{NP}(p)$, A_T and the diagonal elements P_{T11} and P_{T33} of Tanaka's polarization tensor $[P_T]$, for a 90° out-of-phase tension–torsion loading applied to a virgin component, assuming material rates $hr_{NP} = 10$ and $hr_T = 4$. Tension–compression loads induce the tensile element P_{T11} to increase and the torsional element P_{T33} to decrease, while cyclic torsion has the opposite effect. Therefore, the out-of-phase combination of cyclic tension and torsion loads makes both P_{T11} and P_{T33} and therefore A_T oscillate with the same frequency of the applied load history, see Fig. 4. If the normal and effective shear stress amplitudes are equal, i.e. if $\Delta\sigma_x/2 = (\Delta\tau_{xy}/2)\cdot\sqrt{3}$, then both P_{T11} and P_{T33} converge to the same value 0.5, while A_T converges to $A_T = 1/\sqrt{2}$, as demonstrated in Eq. (18). Clearly, this is the reason why Tanaka introduced the $\sqrt{2}$ factor in its target F_{NPt}, to guarantee that this 90° out-of-phase loading results in a NP factor $F_{NP}(p)$ tending toward the target value $A_T\sqrt{2} = 1$, as desired.

The accumulated plastic strain p needed to settle the values of both $[P_T]$ and A_T in periodic load histories is related to the material hardening rate hr_T. Since their evolution is exponential, it can be estimated that their values should have converged within $1 - exp(-4) \cong 98.2\%$ when $hr_T \cdot p = 4$. For the $hr_T = 4$ used in this example, the settling of P_{T11}, P_{T33} and A_T occurs near $p = 4/hr_T = 1 = 100\%$, as verified in Fig. 4, even though both P_{T11} and P_{T33} remain oscillatory along each cycle under such a NP multiaxial loading history. Note that the NP parameter A_T reached an average value near its target $1/\sqrt{2}$ much before its settling at $p = 1 = 100\%$, which allowed $F_{NP}(p)$ to evolve faster than expected, independently of hr_T. Since the adopted NP hardening rate in that example was $hr_{NP} = 10$, $F_{NP}(p)$ settled near $p = 4/hr_{NP} = 0.4 = 40\%$, see Fig. 4.

However, in general, the settling of the non-proportional factor $F_{NP}(p)$ is influenced both by Tanaka's hr_T and by the non-proportional hr_{NP} hardening rates. Fig. 4 shows the evolution of $F_{NP}(p)$, A_T, P_{T11} and P_{T33} under cyclic torsion, applied for $p \geqslant p_a$ just after uniaxial tension–compression cycles applied in the interval $0 \leqslant p \leqslant p_a$. As in Fig. 3, the normal and effective shear stress amplitudes are equal, i.e. $\Delta\sigma_x/2 = (\Delta\tau_{xy}/2)\cdot\sqrt{3}$. The adopted hardening rate $hr_T = 4$ results in a 98.2% settling of P_{T11}, P_{T33} and A_T near $p = 4/hr_T = 1 = 100\%$, as expected. As seen in Fig. 5, the relatively slow evolution of A_T to reach its zero target value delays the settling of $F_{NP}(p)$ to an accumulated plastic strain much larger than the $p = 0.4 = 40\%$ from Fig. 4, even using the same $hr_{NP} = 2.5\cdot hr_T = 10$ from the 90° out-of-phase tension–torsion example shown in Fig. 4. In practice, $F_{NP}(p)$ settles (within 98.2%) in periodic histories at accumulated plastic strain values p between $(4/hr_{NP})$ and $(4/hr_{NP} + 4/hr_T)$.

Note in Fig. 5 that the peak value reached by $F_{NP}(p)$ also depends on the rates hr_T and hr_{NP}. Low ratios such as $hr_{NP}/hr_T \ll 1$ may underestimate NP hardening effects, resulting in $F_{NP}(p)$ peaks much smaller than the target value $A_T\sqrt{2}$. Moreover, such rates

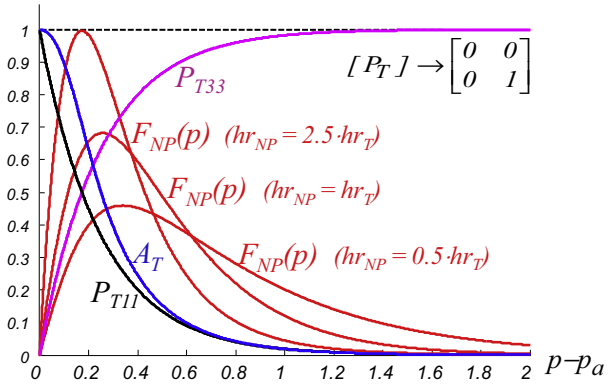

Fig. 5. Evolution of $[P_T]$, A_T and $F_{NP}(p)$ for a cyclic torsion history applied just after uniaxial tension–compression cycles.

$hr_{NP}/hr_T \ll 1$ would imply that the NP hardening effect (whose rate is mainly controlled by hr_{NP}) would only be significant much after the stabilization of the dislocation structures (at a rate controlled by hr_T), not a physically sound hypothesis, since any change in the dislocation structure has an immediate effect on NP hardening behavior. On the other hand, high ratios $hr_{NP}/hr_T > 2.5$ could result in peak values of $F_{NP}(p) \geqslant 1$, violating its definition $0 \leqslant F_{NP}(p) \leqslant 1$. Therefore, it is recommended to fit or calibrate hr_T and hr_{NP} obeying the restriction $hr_T \leqslant hr_{NP} \leqslant 2.5\cdot hr_T$.

Note as well that, except for a few very simple plastic strain paths, Eq. (23) does not have an analytical solution, since the target value $A_T\sqrt{2}$ usually changes at every strain increment following highly non-linear equations that depend on the load path shape. Therefore, maybe except for very simple periodic NP multiaxial load histories, the evolution of $F_{NP}(p)$ can only be calculated through an incremental plasticity algorithm.

Finally, isotropic and NP hardening can be combined using Voce's rule and Eq. (21) into the same model, if their effects are assumed mutually independent, giving the yield surface radius evolution equation

$$S = \underbrace{S_{Yc}\cdot[1+\alpha_{NP}\cdot F_{NP}(p)]}_{\text{NP evolution}} + \underbrace{(S_Y - S_{Yc})\cdot e^{-hr_c\cdot p}}_{\text{isotropic evolution}} \tag{24}$$

where hr_c is a uniaxial strain hardening rate that calibrates the monotonic-to-cyclic hardening transient under uniaxial tension–compression. If the monotonic stress–strain curve is calibrated from Ramberg–Osgood's equation forcing its exponent to be equal to the cyclic exponent h_c, to generate a modified monotonic hardening coefficient H_{mt}, then it is possible to cancel out the 0.002^{h_c} term from the equations $S_Y = H\cdot 0.002^{h_c}$ and $S_{Yc} = H_c\cdot 0.002^{h_c}$, resulting in the evolution of the transient Ramberg–Osgood NP hardening coefficient

$$H(p) = \underbrace{H_c\cdot[1+\alpha_{NP}\cdot F_{NP}(p)]}_{\text{NP evolution}} + \underbrace{(H_{mt} - H_c)\cdot e^{-hr_c\cdot p}}_{\text{isotropic evolution}} \tag{25}$$

4. Estimates of F_{NP} for periodic NP multiaxial load histories

In periodic NP multiaxial histories where each period consists of very few cycles, preventing Tanaka's tensor $[P_T]$ from varying significantly in-between periods, it is expected that $[P_T]$ and $F_{NP}(p)$ converge to approximately constant steady-state values. In this case, integral-based estimates [3,4] or the MOI method [5] could be used to calculate this constant steady-state F_{NP}. In the following sections, two new estimates for the steady-state F_{NP} are proposed, based on Tanaka's transient model.

4.1. Tanaka's NP parameter steady-state estimate

The $F_{NP}(p)$ transient NP hardening equations proposed here, based on Tanaka's model, can also be used to calculate the steady-state F_{NP} of such periodic histories. Integrating Eq. (8) along one of the loading periods and assuming a constant $[P_T]$ with a negligible variation $\Delta[P_T]$ after stabilization, it follows that

$$\int(\vec{n}'\cdot\vec{n}'^T - [P_T])\cdot hr_T\cdot dp = \int d[P_T] = \Delta[P_T] \cong 0 \Rightarrow [P_T] \cong \frac{hr_T\cdot\int\vec{n}'\cdot\vec{n}'^T\cdot dp}{hr_T\cdot\int dp} \tag{26}$$

Tanaka's tensor $[P_T]$ can be assumed approximately constant as long as $hr_T\cdot p \ll 1$, where p is the accumulated plastic strain integrated along one loading period, resulting in

$$[P_T] \cong (1/p)\cdot \int \vec{n}'\cdot\vec{n}'^T\cdot dp,\ \text{where } p=\int dp \tag{27}$$

which is independent of the hardening rate hr_T. Tanaka's tensor $[P_T]$ can then be interpreted as an integral of the directionality matrices $\vec{n}'\cdot\vec{n}'^T$ of the plastic strain directions $\vec{n}'$ weighted by the associated equivalent plastic strain increments dp.

Following the same reasoning, Eq. (23) can be integrated along a full load period assuming a constant $F_{NP}(p)\cong F_{NP}$ with a negligible variation ΔF_{NP} after stabilization, as long as $hr_{NP}\cdot p \ll 1$, resulting in a steady-state estimate for F_{NP} independent of hr_{NP}:

$$\int \left(A_T\sqrt{2}-F_{NP}\right)\cdot hr_{NP}\cdot dp=\int dF_{NP}=\Delta F_{NP}\cong 0\Rightarrow F_{NP} \cong (1/p)\cdot\int A_T\sqrt{2}\cdot dp \tag{28}$$

In a discrete formulation, where the history path is simulated or measured at small finite accumulated plastic strain increments Δp instead of continuously following infinitesimal increments dp, generating thus a polygonal plastic strain path, the steady-state value F_{NP} can be calculated from the *NP Parameter Steady-State* (SS) estimate

$$F_{NP}\cong\frac{1}{p}\cdot\sum A_T\sqrt{2}\cdot\Delta p \tag{29}$$

where the total accumulated plastic strain $p=\sum\Delta p$, Tanaka's tensor $[P_T]\cong\frac{1}{p}\cdot\sum\vec{n}'\cdot\vec{n}'^T\cdot\Delta p$, and Tanaka's NP parameter A_T is given by Eq. (13).

4.2. Rectangular plastic strain path example

Let's apply the above estimate to obtain the steady-state F_{NP} of a plastic strain history that describes a rectangle centered at the origin of the $e_{1pl}\times e_{3pl}$ plastic strain diagram, with sides $2a$ and $2b$ (with $a\geqslant b$), caused by a $\sigma_x\times\tau_{xy}$ tension–torsion history.

The $e_{1pl}\times e_{3pl}$ diagram is equivalent to the von Mises plastic strain diagram $\varepsilon_{xpl}\times\gamma_{xypl}/\sqrt{3}$ scaled up by a factor (3/2), since $e_{1pl}\equiv(3/2)\cdot\varepsilon_{xpl}$ and $e_{3pl}\equiv\gamma_{xypl}\cdot\sqrt{3}/2=(3/2)\cdot(\gamma_{xypl}/\sqrt{3})$. However, this $\varepsilon_{xpl}\times\gamma_{xypl}/\sqrt{3}$ diagram would not be convenient to represent the plastic strain history in this case, because the description of the actual path would require the 4D diagram $\varepsilon_{xpl}\times\varepsilon_{ypl}\times\varepsilon_{zpl}\times\gamma_{xypl}/\sqrt{3}$, since the stress condition $\sigma_y=\sigma_z=0$ results in non-zero plastic strain components $\varepsilon_{y_{pl}}=\varepsilon_{z_{pl}}=-0.5\cdot\varepsilon_{x_{pl}}\neq 0$. The $e_{1pl}\times e_{3pl}$ 2D diagram, on the other hand, completely describes this plastic strain path because in this tension–torsion case $e_{2p}\equiv(\varepsilon_{ypl}-\varepsilon_{zpl})\cdot\sqrt{3}/2=0$, while the remaining components of the 5D plastic strain space E_{5p} become $e_{4pl}=e_{5pl}=0$ due to $\gamma_{xzpl}=\gamma_{yzpl}=0$.

Hence, the equivalent plastic strain increments $dp=(2/3)\cdot|d\vec{e}'_{pl}|$ can be fully calculated in this reduced-order $e_{1pl}\times e_{3pl}$ diagram using $d\vec{e}'_{pl}=[\,e_{1pl}\quad e_{3pl}\,]^T$, resulting in an accumulated plastic strain per period equal to $p=(2/3)\cdot(4a+4b)$, where $4a+4b$ is the rectangle perimeter. Assuming a 2D formulation of the plastic strains, each of the two horizontal segments of this load path has a constant outer product $\vec{n}'\cdot\vec{n}'^T$ obtained from $\vec{n}'=[\pm 1\quad 0]^T$ integrated along the equivalent plastic strain variation $\Delta p_h=(2/3)\cdot(2a)=4a/3$, while each of the two vertical segments has $\vec{n}'\cdot\vec{n}'^T$ with $\vec{n}'=[\,0\quad\pm1\,]^T$ integrated along $\Delta p_v=(2/3)\cdot(2b)=4b/3$, resulting in

$$[P_T]\cong\frac{1}{p}\cdot\int\vec{n}'\cdot\vec{n}'^T\cdot dp=\frac{2}{p}\cdot\begin{bmatrix}1&0\\0&0\end{bmatrix}\cdot\frac{4a}{3}+\frac{2}{p}\cdot\begin{bmatrix}0&0\\0&1\end{bmatrix}\cdot\frac{4b}{3}=\begin{bmatrix}a/(a+b)&0\\0&b/(a+b)\end{bmatrix} \tag{30}$$

The NP parameter A_T cannot be assumed constant since it can abruptly change during a load period. It must be calculated from Eq. (13) for each path segment. Since $[P_T]$ is diagonal, its eigenvalues are the diagonal elements $\lambda_{T1}=a/(a+b)$ and $\lambda_{T2}=b/(a+b)$. The trace of $[P_T]^T\cdot[P_T]$ is then equal to $\lambda_{T1}^2+\lambda_{T2}^2=(a^2+b^2)/(a+b)^2$. For the two horizontal segments with $\vec{n}'=[\pm10]^T$,

$$|[P_T]\cdot\vec{n}'|^2=a^2/(a+b)^2\Rightarrow A_T=\sqrt{1-a^2/(a^2+b^2)}=b/\sqrt{a^2+b^2} \tag{31}$$

while for the two vertical segments with $\vec{n}'=[\,0\quad\pm1\,]^T$,

$$|[P_T]\cdot\vec{n}'|^2=b^2/(a+b)^2\Rightarrow A_T=\sqrt{1-b^2/(a^2+b^2)}=a/\sqrt{a^2+b^2} \tag{32}$$

resulting in the estimate

$$F_{NP}\cong\frac{1}{p}\cdot\int A_T\sqrt{2}\cdot dp=\frac{2}{p}\cdot\left[\frac{b\sqrt{2}}{\sqrt{a^2+b^2}}\cdot\frac{4a}{3}+\frac{a\sqrt{2}}{\sqrt{a^2+b^2}}\cdot\frac{4b}{3}\right]=\frac{b}{a}\cdot\frac{2\sqrt{2}}{(1+b/a)\cdot\sqrt{1+(b/a)^2}} \tag{33}$$

Note that this estimate results in the limit cases $F_{NP}=0$ for $b/a=0$, as expected from a proportional multiaxial history, and $F_{NP}=1$ for $b/a=1$. The F_{NP} estimate for the same rectangular plastic strain path obtained in the MOI method studied in [5] is different from the above, but it also results in the same limit cases.

4.3. Eigenvalue steady-state estimate

The previous example suggests that, for 2D histories involving only two stress or strain components, the degree of non-proportionality can be estimated from the ratio $\lambda_{T2}/\lambda_{T1}$ between the second largest eigenvalue λ_{T2} of $[P_T]$ and the largest λ_{T1}, since F_{NP} was indeed calculated as a function of $\lambda_{T2}/\lambda_{T1}=b/a$. From this observation, it becomes evident that there are several similarities between Tanaka's polarization tensor $[P_T]$ and the Rectangular Moment Of Inertia (RMOI) tensor I_r^O from the MOI method [5]: (i) both are 5×5 tensors defined in the same E_{5p} space, with the possibility to represent them under free-surface conditions as 3×3 or 2×2 tensors in reduced-order spaces; (ii) their eigenvectors represent principal directions of plastic straining for the considered $\vec{e}'_{pl}$ path; (iii) their eigenvalues are a measure of the accumulated plastic strain in the direction of the associated eigenvectors; and (iv) in 2D histories, the NP factor F_{NP} can be estimated from the ratio between their two eigenvalues. However, despite their similarities, $[P_T]$ and I_r^O have different formulations, thus have different eigenvalues and eigenvectors.

If extrapolated to general 6D histories represented in the 5D E_{5p} plastic space, the above analogy with the MOI method suggests that the steady-state NP factor could be estimated from the ratio $\lambda_{T2}/\lambda_{T1}$ ($\lambda_{T2}\leqslant\lambda_{T1}$) between the two largest eigenvalues of $[P_T]$, through

$$F_{NP}\cong\sqrt{\lambda_{T2}/\lambda_{T1}}\quad\text{(Tanaka's Eigenvalue SS estimate)} \tag{34}$$

which is called here *Tanaka's Eigenvalue Steady-State* (SS) estimate for F_{NP}. Since this equation neglects any transient effects on the value of F_{NP}, it should only be applied to relatively simple load histories where $[P_T]$ stabilizes to an almost constant tensor, as in most 2D periodic NP histories consisting of few multiaxial cycles per period.

However, for complex multiaxial NP load histories involving significant plastic straining in all six strain components, perhaps

F_{NP} might also be influenced by the three lower remaining eigenvalues λ_{T3}, λ_{T4} and λ_{T5}, provided that they are significantly higher than zero. On the other hand, if plastic straining along the eigenvectors $\vec{v}_{T1}$ and $\vec{v}_{T2}$ associated with λ_{T1} and λ_{T2} is enough to activate cross-slip in all possible directions of the material microstructure, then the effects of the three remaining eigenvalues on F_{NP} might be negligible.

In summary, the two F_{NP} estimates presented in Sections 4.1 and 4.3 for periodic multiaxial NP load histories estimate the steady-state value of Tanaka's tensor $[P_T]$ from Eq. (27). The first estimate, shown in Eq. (28), requires the calculation of an additional integral involving the A_T parameter, or a summation in the discrete version from Eq. (29), while the second estimate from Eq. (34) is simply based on an eigenvalue ratio. The main advantages of these estimates are their integral formulation, which does not require the transient solution of Tanaka's evolution equation in an incremental plasticity formulation, and their independence of the hr_T and hr_{NP} hardening rates, which would not need to be calibrated if only the steady-state F_{NP} and the associated Ramberg–Osgood NP hardening coefficient $H_{NP} = H_c \cdot (1 + \alpha_{NP} \cdot F_{NP})$ are desired.

In fact, for balanced periodic multiaxial NP histories where $F_{NP}(p)$ stabilizes to a constant value F_{NP} without causing any ratcheting or mean stress relaxation effects, an incremental plasticity algorithm could calculate the stress or strain paths assuming that $H(p) = H_{NP}$ since the beginning of the load history (assuming $p = 0$), without having to deal with transient isotropic and NP hardening and thus a yield surface with changing radius. The resulting stress–strain paths would be very similar to the stabilized ones that would be calculated considering all the transient effects, but at a much lower computational cost. This simplified approach is similar to the one adopted in the εN method, where the uniaxial cyclic curve is assumed stabilized with $H(p) = H_c$ since the beginning of the load history, neglecting the uniaxial monotonic-to-cyclic transient.

The main advantage of this transient incremental plasticity calculation using a steady-state value of F_{NP} (assuming it indeed stabilizes, a simplifying hypothesis applicable to many if not most balanced periodic histories, those with $\sigma_m = 0$) is reduction in computational cost, since Eqs. (8) and (13) won't need to be recalculated at each incremental step. Without the need to store and evolve Tanaka's polarization tensor, which in the general case requires a 5×5 matrix to be represented in the simulation software along with its differential equations, computer time can be typically reduced in about half. Moreover, if the transient response of NP hardening can be ignored (e.g. in periodic histories without significant overloads that could cause load interaction effects), then this simplification does not result in any information loss, since the calculated steady-state paths will end up essentially the same as the computationally-costly ones obtained considering the entire transient of Tanaka's polarization tensor.

Note however that the transient response should be fully calculated for unbalanced loadings, where ratcheting or mean stress relaxation can occur. In this case, neglecting hardening or softening transients would compromise the accuracy of the stress or strain path predictions.

5. Experimental validation

The presented NP hardening formulation has been implemented in the ViDa 3D software to predict multiaxial elastoplastic stress–strain relations (see [11] for a description of its 2D version main features, which are retained and expanded in this much improved version). Kinematic hardening can be considered using multi-surface non-linear kinematic (NLK) models from Chaboche et al. [12], Jiang–Sehitoglu [13,14], Ohno–Wang II [15], or Delobelle et al. [16], implemented through a generalized surface translation rule:

$$\vec{v}'_i = \underbrace{\vec{n}' \cdot \Delta r_i}_{\text{Prager–Ziegler}} - \chi_i^* \cdot m_i^* \cdot \gamma_i \cdot \left[\underbrace{\delta_i \cdot \vec{\beta}'_i}_{\text{dynamic recovery}} + \underbrace{(1-\delta_i) \cdot (\vec{\beta}_i'^T \cdot \vec{n}') \cdot \vec{n}'}_{\text{radial return}} \right] \tag{35}$$

where $\vec{v}'_i$ is the translation direction vector for each hardening surface i, $\vec{\beta}'_i$ is its backstress component, $\vec{n}'$ is the current plastic straining unit direction, Δr_i is the difference between the radii of consecutive hardening surfaces, and the scalar functions χ_i^* and m_i^* are defined as

$$\chi_i^* \equiv \left(\frac{|\vec{\beta}'_i|}{\Delta r_i} \right)^{\chi_i} \text{ and } m_i^* \equiv \begin{cases} \left[\vec{\beta}_i'^T \cdot \vec{n}' / |\vec{\beta}'_i| \right]^{m_i}, & \text{if } \vec{\beta}_i'^T \cdot \vec{n}' \geqslant 0 \\ 0, & \text{if } \vec{\beta}_i'^T \cdot \vec{n}' < 0 \end{cases} \tag{36}$$

where χ_i, m_i, γ_i, and δ_i are adjustable ratcheting parameters for each surface. These versatile equations reproduce Chaboche's model setting $\chi_i = \gamma_i = \delta_i = 1$ and $m_i = 0$, Jiang–Sehitoglu's for $\gamma_i = \delta_i = 1$, $m_i = 0$ and adjustable $0 < \chi_i < \infty$, Ohno–Wang II for $\gamma_i = \delta_i = m_i = 1$ and adjustable $0 < \chi_i < \infty$, and Delobelle's for $\chi_i = m_i = 0$ and adjustable $0 < \gamma_i < 1$ and $0 < \delta_i < 1$. The translation direction vectors $\vec{v}'_i$ from each hardening surface are then used to calculate the corresponding surface backstress increments

$$d\vec{\beta}'_i = \begin{cases} p_i \cdot \vec{v}'_i \cdot dp, \text{if} |\vec{\beta}'| < \Delta r_i \\ 0, \text{if} |\vec{\beta}'| = \Delta r_i \end{cases}, \quad i = 1, 2, \ldots, M \tag{37}$$

where p_i are generalized plastic modulus coefficients calibrated for each surface. NP hardening is considered in the simulation by continuously changing the generalized plastic modulus coefficients p_i of each hardening surface i from their initial values $p_i(0)$, through the equation

$$p_i(p) = p_i(0) \cdot [H(p)/H_c]^{1/h_c} \tag{38}$$

where the transient Ramberg–Osgood NP hardening coefficient $H(p)$ has been defined in Eq. (25).

The computer code accuracy should be verified using the same model in both stress and strain control, as recommended in [1]. That is, the stress history should be calculated in the code from a given strain history, and then the computed stresses should be used as input to the same code to predict the original strain history. The residual numerical errors, which should be as small as possible, are assumed as a suitable metric for the code quality. The code accuracy has been verified for all adopted NLK models following this reasonable methodology, but this verification is considered beyond the scope of this paper and will not be further discussed here. However, numerical simulation comparisons with experimental data from Itoh et al. [17] show a better agreement for Jiang–Sehitoglu's model, among all the studied ones.

Tension–torsion experiments are then performed on tubular annealed 316L stainless steel specimens in an MTS tension–torsion testing machine, see Fig. 6. Engineering stresses and strains are measured using a load/torque cell and a MTS axial/torsional extensometer. The cyclic properties of this steel are obtained from traditional uniaxial εN tests, resulting in a calibrated uniaxial cyclic hardening coefficient $H_c = 874$ MPa and exponent $h_c = 0.123$, with Young's modulus $E = 193$ GPa. To improve the calculation accuracy, the backstress is divided into five additive components, following Chaboche's idea [12]. Therefore, the following simulations adopt Jiang–Sehitoglu's kinematic hardening model with five surfaces, i.e. one yield plus four hardening surfaces (not to mention the rupture surface, which does not translate and would constitute a sixth surface).

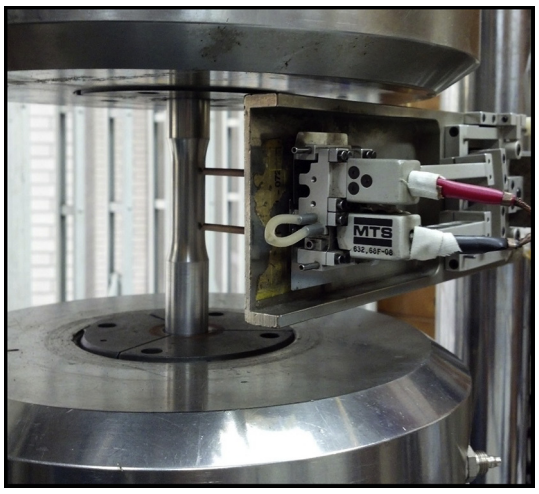

Fig. 6. Tubular tension–torsion specimen mounted in an MTS tension–torsion machine, showing the axial/torsional extensometer.

Using the calibration procedure from [14], for a chosen set of generalized plastic modulus coefficients $p_i = \{6176,\ 786,\ 100,\ 12.7,\ 1.62\}$ MPa for surfaces $i = 1,\ 2, \ldots,\ 5$, respectively, the resulting radii become $r_i \cong \{231, 297, 382, 491, 632\}$ MPa, with differences $\Delta r_i \cong \{66,\ 85,\ 109,\ 141,\ 217\}$ MPa between the radii of consecutive surfaces, where the rupture surface (constant) radius is $r_6 = 849$ MPa. Uniaxial ratcheting experiments are used to calibrate the parameters $X_i = \{1,\ 1,\ 2.9,\ 3,\ 4\}$. An additional hardening coefficient $\alpha_{NP} = 0.86$ is calibrated from 90° out-of-phase tension–torsion circular paths, assuming in this case $F_{NP} = 1$. NP hardening rates are also calibrated in the same way, resulting in NP hardening rates $hr_{NP} = 1.3$ and $hr_T = hr_{NP}/2$.

A thin wall of 1.5 mm is usually adopted in the tubular specimen, to avoid having to deal with stress gradient effects across the thickness. But, since some experiments involved large compression strains, the minimum wall thickness was increased from 1.5 to 2.0 mm to avoid buckling. On the critical section, the tubular specimen has then external $d_{ext} = 16$ mm and internal $d_{int} = 12$ mm diameters.

Note that linear elastic (LE) stress analyses tend to overestimate the elastoplastic stresses especially for specimens with thicker walls, therefore ASTM E2207-08 recommends replacing the term $(d_{ext}^4 - d_{int}^4) = (d_{ext}^2 - d_{int}^2)\cdot(d_{ext}^2 + d_{int}^2)$ from the denominator of the LE expression for the engineering shear stress τ_{xy}^{eng} (due to torsion) with the higher $(d_{ext}^2 - d_{int}^2)\cdot(d_{ext}^2 + d_{ext}\, d_{int})$ to decrease τ_{xy}^{eng}.

The conversion from engineering (eng) to true strains is obtained from

$$\begin{cases} \varepsilon_x = \ln\left(1+\varepsilon_x^{eng}\right) \\ \varepsilon_y = \ln\left(1+\varepsilon_y^{eng}\right) \\ \varepsilon_z = \ln\left(1+\varepsilon_z^{eng}\right) \end{cases} \text{and} \begin{cases} \gamma_{xy} \cong \tan^{-1}\left(\gamma_{xy}^{eng}\right) \\ \gamma_{xz} \cong \tan^{-1}\left(\gamma_{xz}^{eng}\right) \\ \gamma_{yz} \cong \tan^{-1}\left(\gamma_{yz}^{eng}\right) \end{cases} \tag{39}$$

But the conversion from engineering to true stresses requires a general multiaxial formulation that incorporates Poisson effects in all directions, based on the equations

$$\begin{cases} \sigma_x = \sigma_x^{eng}/\left[(1+\varepsilon_y^{eng})\cdot(1+\varepsilon_z^{eng})\right] \\ \sigma_y = \sigma_y^{eng}/\left[(1+\varepsilon_x^{eng})\cdot(1+\varepsilon_z^{eng})\right] \\ \sigma_z = \sigma_z^{eng}/\left[(1+\varepsilon_x^{eng})\cdot(1+\varepsilon_y^{eng})\right] \\ \tau_{xy} = \tau_{xy}^{eng}/\left[(1+\varepsilon_y^{eng})\cdot(1+\varepsilon_z^{eng})\right] = \tau_{yx} = \tau_{yx}^{eng}/\left[(1+\varepsilon_x^{eng})\cdot(1+\varepsilon_z^{eng})\right] \\ \tau_{xz} = \tau_{xz}^{eng}/\left[(1+\varepsilon_y^{eng})\cdot(1+\varepsilon_z^{eng})\right] = \tau_{zx} = \tau_{zx}^{eng}/\left[(1+\varepsilon_x^{eng})\cdot(1+\varepsilon_y^{eng})\right] \\ \tau_{yz} = \tau_{yz}^{eng}/\left[(1+\varepsilon_x^{eng})\cdot(1+\varepsilon_z^{eng})\right] = \tau_{zy} = \tau_{zy}^{eng}/\left[(1+\varepsilon_x^{eng})\cdot(1+\varepsilon_y^{eng})\right] \end{cases} \tag{40}$$

Note that the force F_{yx} that causes the engineering shear stress τ_{yx}^{eng} is in general different from the F_{xy} that causes τ_{xy}^{eng}, because the equilibrium of moments in a deformed element of lengths x and y requires that the moment $F_{xy}\cdot(x/2)$ caused by F_{xy} with respect to the element centroid has the same magnitude as the moment $F_{yx}\cdot(y/2)$ caused by F_{yx}. But, even though in general $\tau_{xy}^{eng} \neq \tau_{yx}^{eng}$ for engineering shear stresses, the tensor symmetry condition $\tau_{xy} = \tau_{yx}$ must be satisfied for true shear stresses to guarantee static equilibrium.

Strain-controlled tension–torsion tests are then performed adopting strain paths describing square paths in the $\varepsilon_x \times \gamma_{xy}/\sqrt{3}$ diagram. Fig. 7(left) shows applied square strain paths with normal amplitudes 0.2%, 0.4%, 0.6% and 0.8%. Fig. 7(right) shows the measured stress paths during the entire NP hardening transient for all applied strain levels, and the corresponding predictions performed using the presented formulation of Tanaka's NP hardening model together with Jiang–Sehitoglu's kinematic hardening model, resulting in a good agreement, within 78 MPa RMS (less than 10% of the maximum stress levels). Fig. 8 shows the normal and shear hysteresis loops associated with the paths from Fig. 7. Note that Tanaka's model predicts that F_{NP} converges to 1.0 for square paths, overestimating the normal and especially the shear stresses; these experiments suggest F_{NP} tending to a slightly lower value, near 0.9.

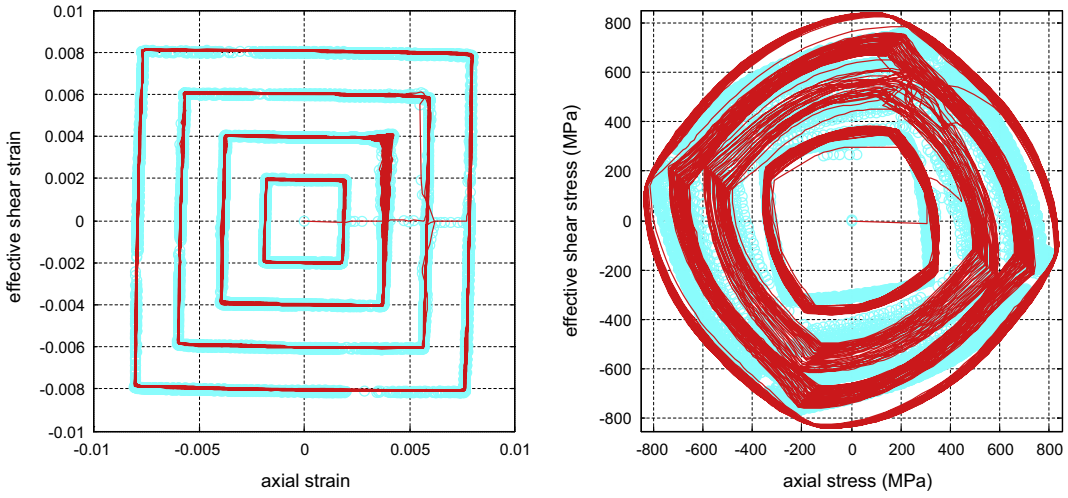

Fig. 7. Left: square $\varepsilon_x \times \gamma_{xy}/\sqrt{3}$ strain paths applied to the tension–torsion tubular specimens with amplitudes 0.2%, 0.4%, 0.6% and 0.8%; Right: resulting $\sigma_x \times \tau_{xy}\sqrt{3}$ stress paths experimentally measured (light lines) and predicted using the simulator (dark lines).

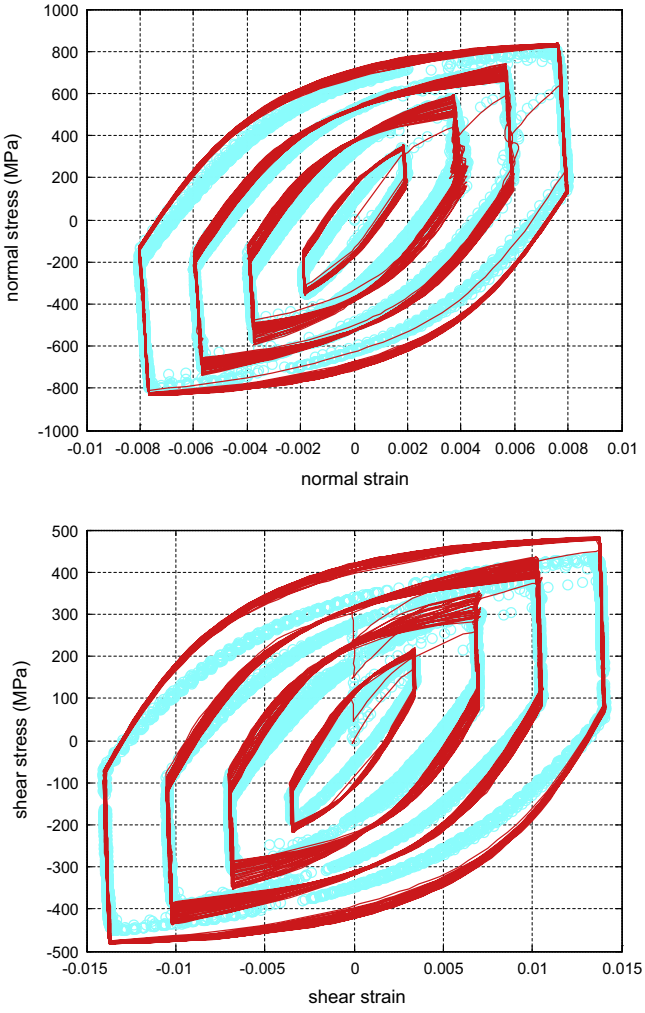

Fig. 8. Normal and shear hysteresis loops from square strain histories, either experimentally measured (light lines) or predicted using the simulator (dark lines).

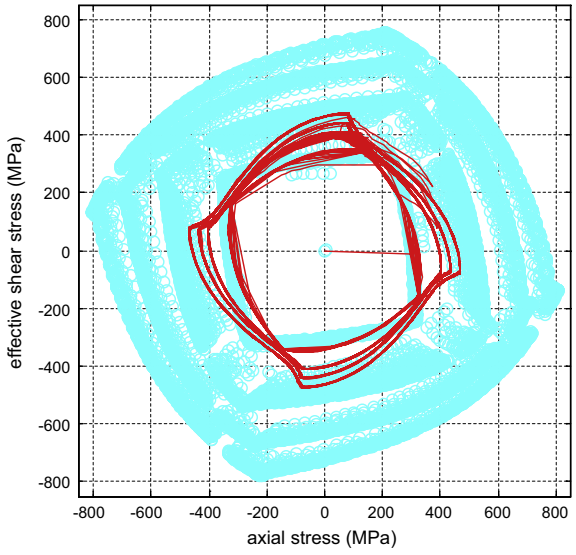

Fig. 9. Wrong $\sigma_x \times \tau_{xy}\sqrt{3}$ stress paths that would be predicted using the simulator neglecting NP hardening effects (dark lines), and the actual experimentally measured paths (light lines).

As expected, the proposed NP parameter steady-state estimate exactly coincided with the steady-state value of the transient Tanaka model, obtained from the simulations. Due to the symmetry of the considered square path, the proposed eigenvalue steady-state estimate also coincided with Tanaka's transient predictions after stabilization, however for asymmetric paths these values could be somewhat different. Further investigation is required to evaluate these probably small differences between the two proposed steady-state estimates.

Finally, Fig. 9 shows the wrongfully predicted stress path if NP hardening is ignored. Note the enormous influence of NP hardening in the resulting stress ranges, which would be higher than the wrong predictions by, in average, 5% for the 0.2% strain amplitudes (where plastic strains are still small), by 45% for 0.4% amplitudes, by 65% for 0.6%, and up to 75% (in average) for 0.8%. Multiaxial fatigue calculations cannot ignore these significant hardening effects: for instance, Smith–Watson–Topper's damage parameter would be underestimated by a factor of up to 1.85 in some of the highest amplitude cycles, resulting in highly non-conservative fatigue life predictions.

6. Conclusions

In this work, Tanaka's incremental plasticity model was presented in a special 5D plastic strain space, from which an evolution equation for the non-proportionality factor F_{NP} was obtained, as a function of the accumulated plastic strain p. It was shown that the eigenvectors of Tanaka's polarization tensor represent principal directions along which dislocation structures may form, while the eigenvalues quantified them. Two new integral estimates for the steady-state F_{NP} of periodic load histories were proposed. The presented equations were validated from non-proportional tension–torsion experiments with 316L steel tubular specimens.

Acknowledgments

This work was supported in part by the National Natural Science Foundation of P.R. China under Grant No. 11302150. CNPq-Brazil provided fellowships for Profs. Meggiolaro, M.A. and Castro, J.T.P.

References

[1] Socie DF, Marquis GB. Multiaxial fatigue. SAE; 1999.
[2] Bannantine J.A., Socie, D.F. A variable amplitude multiaxial fatigue life prediction method. Fatigue under biaxial and multiaxial loading, vol. 10. ESIS Publication; 1991. p. 35–51.
[3] Itoh T, Sakane M, Ohnami M, Socie DF. Nonproportional low cycle fatigue criterion for type 304 stainless steel. ASME J Eng Materials Technol 1995;117:285–92.
[4] Bishop JE. Characterizing the non-proportional and out-of-phase extent of tensor paths. Fatigue Fract Eng Mater Struct 2000;23:1019–32.
[5] Meggiolaro MA, Castro JTP. Prediction of non-proportionality factors of multiaxial histories using the moment of inertia method. Int J Fatigue 2014;61:151–9.
[6] Tanaka E. A nonproportionality parameter and a cyclic viscoplastic constitutive model taking into account amplitude dependences and memory effects of isotropic hardening. Eur J Mech A Solids 1994;13:155–73.
[7] Kanazawa K, Miller K, Brown M. Cyclic deformation of 1% Cr–Mo–V steel under out-of-phase loads. Fatigue Fract Eng Mater Struct 1979;2:217–28.
[8] Safaei M, Zang S-L, Lee MG, Waele WD. Evaluation of anisotropic constitutive models: mixed anisotropic hardening and non-associated flow rule approach. Int J Mech Sci 2013;73:53–68.
[9] Meggiolaro MA, Castro JTP. An improved multiaxial rainflow algorithm for non-proportional stress or strain histories – Part I: enclosing surface methods. Int J Fatigue 2012;42:217–26.
[10] Meggiolaro MA, Castro JTP. An improved multiaxial rainflow algorithm for non-proportional stress or strain histories – Part ii: the modified wang brown method. Int J Fatigue 2012;42:194–206.
[11] Meggiolaro MA, Castro JTP. Automation of the fatigue design under variable amplitude loading using the ViDa software. Int J Struct Integrity 2010;1:1–6.

[12] Chaboche JL, Dang Van K, Cordier G. Modelization of the strain memory effect on the cyclic hardening of 316 stainless steel. In: Transactions of the fifth international conference on structural mechanics in reactor technology, Div. L, Berlin; 1979.
[13] Jiang Y, Sehitoglu H. Modeling of cyclic ratchetting plasticity, Part I: development of constitutive relations. ASME J Appl Mech 1996;63(3):720–5.
[14] Jiang Y, Sehitoglu H. Modeling of cyclic ratchetting plasticity, Part II: comparison of model simulations with experiments. ASME J Appl Mech 1996;63(3):726–33.
[15] Ohno N, Wang JD. Kinematic hardening rules with critical state of dynamic recovery, part I: formulations and basic features for ratchetting behavior. Int J Plast 1993;9:375–90.
[16] Delobelle P, Robinet P, Bocher L. Experimental study and phenomenological modelization of ratchet under uniaxial and biaxial loading on an austenitic stainless steel. Int J Plast 1995;11:295–330.
[17] Itoh T, Sakane M, Ohnami M, Socie DF. Nonproportional low cycle fatigue criterion for type 304 stainless steel. ASME J Eng Mater Technol 1995;117:285–92.